Correlating Changes in Spot Filling Factors with Stellar Rotation: The Case of LkCa 4

Facundo Pérez Paolino[1] , Jeffrey S. Bary[1,2] , Michael S. Petersen[2,3] , Kimberly Ward-Duong[2,4] ,
Benjamin M. Tofflemire[5,8] , Katherine B. Follette[6] , and Heidi Mach[7]
[1] Colgate University, 13 Oak Drive, Hamilton, NY 13346, USA; jbary@colgate.edu
[2] Visiting astronomer at the NASA Infrared Telescope Facility, Mauna Kea Access Road, Hilo, HI 96720, USA[9]
[3] Institute for Astronomy, University of Edinburgh, Royal Observatory, Blackford Hill, Edinburgh EH9 3HJ, UK
[4] Department of Astronomy, Smith College, 10 Elm Street, Northampton, MA 01063, USA
[5] Department of Astronomy, The University of Texas at Austin, Austin, TX 78712, USA
[6] Department of Physics and Astronomy, Amherst College, Amherst, MA 01003, USA
[7] Allegheny College, 520 N. Main Street Meadville, PA 16335, USA

Abstract

We present a multi-epoch spectroscopic study of LkCa 4, a heavily spotted non-accreting T Tauri star. Using SpeX at NASA's Infrared Telescope Facility (IRTF), 12 spectra were collected over five consecutive nights, spanning ≈1.5 stellar rotations. Using the IRTF SpeX Spectral Library, we constructed empirical composite models of spotted stars by combining a warmer (photosphere) standard star spectrum with a cooler (spot) standard weighted by the spot filling factor, $f_{\rm spot}$. The best-fit models spanned two photospheric component temperatures, $T_{\rm phot} = 4100$ K (K7V) and 4400 K (K5V), and one spot component temperature, $T_{\rm spot} = 3060$ K (M5V) with an A_V of 0.3. We find values of $f_{\rm spot}$ to vary between 0.77 and 0.94 with an average uncertainty of ~0.04. The variability of $f_{\rm spot}$ is periodic and correlates with its 3.374 day rotational period. Using a mean value for $f_{\rm spot}^{\rm mean}$ to represent the total spot coverage, we calculated spot corrected values for $T_{\rm eff}$ and $L_\star$. Placing these values alongside evolutionary models developed for heavily spotted young stars, we infer mass and age ranges of 0.45–0.6 $M_\odot$ and 0.50–1.25 Myr, respectively. These inferred values represent a twofold increase in the mass and a twofold decrease in the age as compared to standard evolutionary models. Such a result highlights the need for constraining the contributions of cool and warm regions of young stellar atmospheres when estimating $T_{\rm eff}$ and $L_\star$ to infer masses and ages as well as the necessity for models to account for the effects of these regions on the early evolution of low-mass stars.

Unified Astronomy Thesaurus concepts: T Tauri stars (1681); Star formation (1569); Early stellar evolution (434); Starspots (1572); Pre-main sequence stars (1290); Stellar evolutionary tracks (1600)

1. Introduction

Accurate age determinations for pre-main-sequence (PMS) stars are essential to understanding the formation and evolution of stars and planetary systems. One popular method for constraining the ages of PMS stars relies on a direct comparison between the observed stellar luminosities and surface temperatures and those predicted by theoretical evolutionary models (e.g., D'Antona & Mazzitelli 1994; Soderblom et al. 2014; Baraffe et al. 2015). Unfortunately, young stars are complex systems often characterized by strong magnetic fields, rapid rotation rates, excess emission from circumstellar material, mass accretion onto the stellar surfaces, and mass outflow from disk and stellar winds (e.g., Hartmann et al. 2016). Chromospheric and coronal activity are heightened, leading to strong flares producing large fluxes of high-energy photons (e.g., Feigelson & Montmerle 1999; Petrov et al. 2011). As part of the heightened activity, the large-scale inhibition of convection by strong magnetic fields in these

systems is quite possible, resulting in the formation of starspots covering significant fractions of the stellar surfaces. Given the episodic or transient nature of these phenomena, young stellar systems exhibit variability on timescales as short as hours across all wavelengths. Such activity often limits our ability to constrain otherwise straightforward observable stellar parameters. Ages inferred from comparisons of effective temperatures and stellar luminosities to those predicted by standard evolutionary models (e.g., Baraffe et al. 2015) typically result in large spreads in the ages of stars residing in the same cluster. While some of this spread may be due to different star formation epochs that have occurred within the same region, ignoring the effects of spots on the observable quantities and on stellar evolution likely contributes to this spread, confusing our understanding of the star-forming history. Therefore, the presence of large starspots on the surfaces of a sizable fraction of young stars and the lack of evolutionary models that account for spots are potentially responsible for some of the spread in the ages, masses, and evolutionary statuses inferred for stars in a given young cluster (Preibisch 2012; Soderblom et al. 2014).

Large complexes of cool spots rotating with the surfaces of low-mass PMS stars produce periodic variability, which can be used profitably to measure rotation periods for these objects (e.g., Bouvier et al. 1995; Herbst et al. 2007; Grankin et al. 2008). Such spots also provide a reasonable explanation for the systematic color anomalies and optical/infrared spectral type mismatches observed for T Tauri stars, both accreting and non-accreting (Gullbring et al. 1998; Vacca & Sandell 2011;

Debes et al. 2013; Bary & Petersen 2014; Czekala et al. 2015; Kastner et al. 2015; Gully-Santiago et al. 2017).

Debes et al. (2013) and Bary & Petersen (2014) demonstrate that the near-infrared (NIR) spectra of TW Hya and DQ Tau, respectively, can be modeled with empirical composite spectra made from a weighted average of two standard star spectra—a warmer standard representing the photosphere and a cooler one representing the spot. In both cases, the authors find that cool spots may cover over 50% of the surfaces of the stars. Donati et al. (2014) use multi-epoch spectropolarimetric observations ($R \sim 65{,}000$) of LkCa 4, a weak-line T Tauri star and the subject of the study presented herein, to construct tomographic maps of the stellar surface and to study the magnetic topology of the star. Their results indicate the presence of large cool spots covering more than 20% of the surface as well as the existence of large warm plages. Herczeg & Hillenbrand (2014) use TiO features in the NIR to revise the spectral type of LkCa 4 from a K7 to a later M1.5, likely highlighting the effect of spots on single-band temperature measurements. Gully-Santiago et al. (2017, hereafter GS17) also observe LkCa 4 at high-spectral resolution ($R \sim 45{,}000$) in the NIR with IGRINS. Applying a two-temperature atmospheric model to fit their data as well as the TiO bands in the spectra of Donati et al. (2014), GS17 establish the presence of a large spot or spot complex that covers nearly 80% of the stellar surface. The surprisingly large discrepancy between filling factors determined by Donati et al. (2014) and GS17 can be reconciled by the fact that the Zeeman Doppler imaging (ZDI) technique employed by Donati et al. is insensitive to collections of smaller spots.

Using high-resolution iSHELL spectra ($R \sim 47{,}000$), Flores et al. (2019, 2022) measure magnetic field strengths on the surfaces of T Tauri stars and correlate magnetic field strengths to measurements of stellar temperatures. The results of Flores et al. indicate that a correlation likely exists between spots and effective temperatures of these sources.

Collectively, these studies highlight the uncertainty and complexity that starspots introduce when using evolutionary models to infer ages and masses of highly active PMS stars. They also illustrate the importance of developing new evolutionary models of spotted stars, incorporating the physical mechanisms that produce the spots as well as predicting their impact on the evolution of young stars (e.g., Feiden 2016; Somers et al. 2020). Such models will improve our efforts to confidently and accurately infer the ages of PMS stars and the clusters in which they form. Constraining these models will require a simple and direct method for determining spot filling factors and spot temperatures for large samples of PMS stars across the mass spectrum.

Toward this goal, we present a multi-epoch, medium-resolution, NIR spectroscopic study of LkCa 4 in which we constrain spot sizes and temperatures and correlate the changes in the spot filling factors with the rotational phase of the star. Using our best-fit model parameters for photospheric temperature (T_{phot}), spot temperature (T_{spot}), and spot filling factors (f_{spot}), we are able to reproduce the V-band variability observed during a time frame that overlaps with our spectral observations. We show how our results compare with the studies mentioned above, which were conducted at much higher spectral resolution (Donati et al. 2014; GS17). The observations presented benefit from consistent temporal coverage over five consecutive nights or roughly 1.5 stellar rotations.

Although the absolute value of the total spot coverage depends on the model-dependent photosphere and spot temperatures, the temporal coverage permits us to better constrain the total fraction of the stellar surface covered by spots than that of a single observation.

First, we outline the observations and calibration steps in Section 2. In Sections 3 and 3.1, we describe the empirical composite spectral models and determine the best-fit filling factors and temperature ranges for the photosphere and the spots. In Section 3.2, we present the strong correlation we find between the photometric variability and the changes observed in the spot filling factors suggesting our observations and spectral models are sensitive to the rotation of the star. In Section 4, we take a small digression to explore another spectral type indicator, the D_{CO} spectral index based on the 2.29 μm CO bandhead (Mármol-Queraltó et al. 2008) to test its sensitivity to spots and its consistency with other temperature indicators. In Section 5, we use the best-fit model parameters to calculate spot-corrected T_{eff} and $L_{\star}$. We then place these spot-corrected values on the H–R diagram alongside evolutionary tracks and isochrones predicted by both standard and spotted star evolutionary models (Baraffe et al. 2015; Somers et al. 2020) and discuss the results.

2. Observations

We observed LkCa 4 using SpeX, a medium-resolution cross-dispersed NIR spectrograph at NASA's Infrared Telescope Facility (IRTF) atop Maunakea over five consecutive nights on UT 2019 January 6–10. Using the short-wavelength cross-dispersed mode (SXD; Rayner et al. 2003) with the $0\farcs3 \times 15''$ slit ($R \sim 2000$), we collected a total of 12 spectra of the target as part of a larger program to study starspots and accretion activity in PMS systems. The SXD setting provides continuous wavelength coverage from 0.7–2.55 μm. The goals of this project were achieved due to favorable weather conditions, which permitted consistent monitoring of more than one full rotation of LkCa 4.

The data were collected using an AB nod sequence typical of long-slit NIR spectra acquisition. The subtraction of the 2D spectral image pairs allows for the efficient removal of terrestrial OH emission lines, background, and dark current. A0V telluric standards HD 27761 and HD 24000 were observed close in airmass ($\Delta sz \leqslant 0.1$) to the target and were used to remove telluric absorption features and to calibrate the target spectra. Flat-field corrections, wavelength calibrations, spectral extraction, co-adding, telluric corrections, and merging of the spectral orders were performed using SpexTool v4.0.5, an IDL-based reduction package described by Cushing et al. (2004). Details of the observations can be found in Table 1. Sample spectra covering the 0.8–1.35 μm region are shown in Figure 1, highlighting the nature of the variability observed in the shorter wavelength regions of the spectra.

3. Empirical Models of Spotted Stars

We constructed two-temperature models of spotted stars as empirical composite spectra following the same procedure outlined in Debes et al. (2013) and Bary & Petersen (2014). We use the term empirical composite to clearly indicate that these model spectra are not generated from synthetic stellar atmospheric models. Instead, they are produced using the spectra of standards found in the SpeX IRTF Library (Cushing et al. 2005;
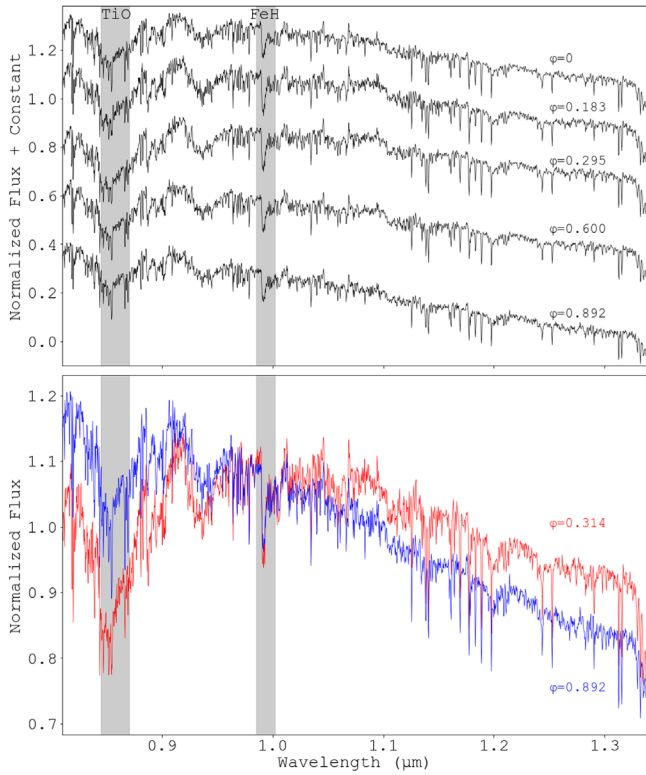
Figure 1. (Top) Five partial LkCa 4 SpeX spectra are plotted from 0.8–1.35 μm; one from each night of the observing run. The spectra have been normalized by their mean flux values in the plotted wavelength range and shifted by adding a constant for display purposes. Changes in the strengths of TiO and FeH absorption bands are apparent, as well as variations in the overall spectral shapes. Gray-shaded areas highlight the spot-sensitive TiO and FeH features. (Bottom) Two LkCa 4 spectra plotted at maximum (red) and minimum (blue) excursions from the average spectrum.

Table 1
LkCa 4 SpeX Observations

UT Date Time	Airmass (s z)	Exposure Time (s × n Co-adds)	Telluric Standard	Δs z
Jan 6 05:07:28	1.222	75 × 8	HD 24000	0.10
Jan 6 07:24:35	1.012	…	HD 24000	0.01
Jan 6 09:29:46	1.122	…	HD 27761	0.03
Jan 7 04:59:00	1.237	…	HD 24000	0.11
Jan 7 06:35:23	1.038	…	HD 24000	0.02
Jan 8 05:43:50	1.108	…	HD 24000	0.06
Jan 8 07:19:17	1.011	…	HD 27761	0.01
Jan 8 10:06:01	1.246	…	HD 27761	0.05
Jan 9 05:19:47	1.153	…	HD 24000	0.07
Jan 9 07:07:34	1.013	150 × 4	HD 27761	0.01
Jan 10 04:55:55	1.209	…	HD 24000	0.10
Jan 10 07:02:14	1.014	…	HD 27761	0.01

Rayner et al. 2009). In the two-temperature models, the spectrum of the warmer standard represents the photosphere, $F_\lambda(T_{phot})$, and the cooler standard represents the spots, $F_\lambda(T_{spot})$. Therefore, changing model parameters T_{phot} or T_{spot} is achieved by selecting different spectral standards from the SpeX Library. The composite spectral models are generated using the following:

$$F_{\lambda,model} = F_\lambda(T_{phot})(1 - f_{spot}) + F_\lambda(T_{spot})f_{spot} C_{bb} \qquad (1)$$

where $F_\lambda(T_{phot})$ and $F_\lambda(T_{spot})$ are normalized template spectra, f_{spot} is the instantaneous spot filling factor (i.e., the fraction of

Table 2
SpeX Spectral Standards

Star	Spectral Type	T_{eff}[a]	Variable	$E(B - V)$[b]
HD 45977	K4V$_p$	4600	None	0.012
HD 36003	K5V$_p$	4400	None	−0.037
HD 237903	K7V$_p$	4100	None	0.022
HD 19305	M0V$_p$	3850	None	<0.019
HD 42581	M1V$_s$	3660	UV[c]	<0.018
Gl 806	M2V$_s$	3560	var[d]	…
Gl 388	M3V$_s$	3430	UV[e]	<0.009
Gl 213	M4V$_s$	3210	BY[f]	<0.009
Gl 51	M5V$_s$	3060	UV[e]	…
Gl 406	M6V$_s$	2810	UV[f]	0.063
Gl 644C	M7V$_s$	2680	UV[c]	0.100
LP 412-31	M8V$_s$	2570	UV[g]	…

Notes.
[a] All temperatures are from Pecaut & Mamajek (2013).
[b] Color excesses reported in Rayner et al. (2009).
[c] Gershberg et al. (1999).
[d] Uncharacterized variability. (Alfonso-Garzon et al. 2012).
[e] Jones & West (2016).
[f] Samus' et al. (2017).
[g] Stelzer et al. (2006).

the observable stellar surface that is covered by spots following the convention adopted by GS17), and C_{bb} is a scaling constant defined as the ratio of the Planck functions of the photosphere and the spot at 1.1 μm. C_{bb} approximates the relative normalized flux units of the two spectra based on their effective temperatures. Before combining, the wavelength arrays of the standard star spectra are aligned through a one-dimensional interpolation using the interp1d algorithm found in SciPy (Jones et al. 2001). The resulting composite model spectrum is renormalized before fitting to the target spectra.

We have chosen to use dwarf spectral standards when constructing the models similar to Debes et al. (2013) and Bary & Petersen (2014). The spectral standards used to construct the spotted star models as well as the spectral types, effective temperatures, variability status, and $B - V$ color excesses for each source are listed in Table 2. We note that M dwarfs are well known for their aperiodic variability due to strong stochastic flares (Hartman et al. 2011). We find that six of the M dwarf standards selected to represent the spots are identified as eruptive variables. However, we proceed with using the M dwarfs as standards assuming that the short-lived nature of the eruptions is not likely to impact the single-epoch observations presented in the SpeX library. Rayner et al. (2009) measure color excesses for the library stars and do not present dereddened spectra for stars with $E(B - V) < 0.108$. The color excesses quoted for Gl 406 (M6V) and Gl 466C (M7V) are significant. Therefore, these standard star spectra were dereddened with a standard interstellar extinction law (Fitzpatrick 1999) prior to using them to construct spectral models.

In general, optical and infrared TiO and FeH features are temperature sensitive and are considered good, yet complicated spot indicators (Herbst & Levreault 1990; Neff et al. 1995; O'Neal et al. 1996; Schiavon et al. 1997). Therefore, it is important to note different sensitivities between TiO and FeH that may impact the individual constraints they place on the best-fit composite spectra and values for f_{spot}. For instance, the FeH Wing-Ford band at 0.99 μm is sensitive to changes in

surface gravity with the feature appearing to be strongest in the spectra of the coolest dwarf stars (Schiavon et al. 1997). In fact, its presence and strength in NIR spectra of unresolved stellar populations have frequently been used to measure the contribution from cool, dwarf stars (e.g., Couture & Hardy 1993; Schiavon et al. 1997; Cenarro et al. 2003). However, with regards to its sensitivity to small changes in log g, Bary & Petersen (2014) found little difference in the strengths of FeH between synthetic spectra of a K5IV with log $g = 3.5$, representing a *puffy* T Tauri star, and a K5V dwarf star with log $g = 4.5$ (Coelho et al. 2005). Such a similarity likely indicates that larger differences in the surface gravity are required to produce an effect on the FeH band strengths to be detectable with moderate resolution spectroscopy.

In addition to surface gravity effects, the magnetic sensitivities of both TiO and FeH molecular states and transitions to Zeeman effects is also an important consideration. Absorption features associated with both bands have been shown to be quite sensitive to magnetic fields and have been used to measure magnetic field strengths on K- and M-type stars (e.g., Afram & Berdyugina 2015). FeH has gained considerable attention as a probe of magnetic field strengths on M dwarfs, which are too cool to possess strong, magnetically sensitive atomic features (Valenti & Johns-Krull 2001; Reiners & Basri 2006; Shulyak et al. 2014; Afram & Berdyugina 2019; Kochukhov 2021).

Given that the composite spectra are constructed with template spectra of M dwarfs representing the cooler spotted regions that likely possess magnetic fields that are stronger than the non-spot regions, it is important to acknowledge that the M dwarf templates possess TiO and FeH features that are affected by strong magnetic fields. For instance, Afram & Berdyugina (2019) find a range of 3–6 kG fields with an average of 5 kG for a sample of nine M1-7 dwarfs. Shulyak et al. (2019) measure magnetic fields for a larger sample of 29 active M dwarfs and similarly find field strengths in the 1–7 kG range. On average, these M dwarfs have greater field strengths than the 0.71–3.24 kG range measured by Flores et al. (2022) for a sample of 40 K and M spectral type T Tauris stars. The TiO and FeH contributions to the composite spectra from the M dwarf templates will likely incorporate some effects of a magnetic field within the 1–7 kG range.

Previous studies of spotted T Tauri stars have indicated that the spectral types representing $T_{\rm phot}$ in two-temperature models will be similar to the optically derived spectral types for the stars (Debes et al. 2013; Bary & Petersen 2014; Herczeg & Hillenbrand 2014; GS17). Therefore, the spectral templates chosen to represent $F_\lambda(T_{\rm phot})$ in our composite models bracket the K7V spectral type reported for LkCa 4 in the literature (Herbig et al. 1986; Strom & Strom 1994; Hartigan et al. 1995; White & Ghez 2001; Grankin 2013). We constrained the parameter $F_\lambda(T_{\rm phot})$ by selecting four photospheric templates: M0V$_p$, K7V$_p$, K5V$_p$, and K4V$_p$ (3850 K $\leqslant T_{\rm phot} \leqslant$ 4600 K). The spectral types of the templates representing $F_\lambda(T_{\rm spot})$ were confined to the range between M8V$_s$ and M1V$_s$ (2570 K $\leqslant T_{\rm spot} \leqslant$ 3660 K). This range of spot temperatures encompasses the values suggested by previous studies (i.e., GS17) and fits the typical spot-to-photosphere temperature ratios (Strassmeier 2009; Fang et al. 2018). The contribution of the spot template to the composite spectrum is weighted by the spot filling factor, $f_{\rm spot}$, which we allow to vary from 0.0 to 1.0. It is important to note that cooler spots with smaller filling

factors will mimic warmer spots with larger filling factors leading to an inherent degeneracy in these models.

3.1. Model Fitting

We searched for the best-fit model for each of the 12 epochs of LkCa 4 spectra by varying four model parameters: $T_{\rm phot}$, $T_{\rm spot}$, $f_{\rm spot}$, and A_V. The values for $T_{\rm phot}$, $T_{\rm spot}$ and $f_{\rm spot}$ were constrained by the parameter space defined above in Section 3. We let A_V vary between 0.0 and 1.0 in steps of 0.1 to encompass the two values of 0.35 (GS17) and 0.69 (Kenyon & Hartmann 1995) reported in the literature. The LkCa 4 spectra were dereddened with the same standard interstellar extinction law used for the M dwarf standards.

We selected three spectral windows to constrain the best-fit models. The first is a broad spectral window stretching from 0.8^{10}–1.35 μm, which we will designate $F_{0.8-1.35\ \mu m}$. The large wavelength coverage of this window will force the best-fit models to accurately reproduce the shape of the continuum in a region of the spectrum that is most significantly affected by interstellar reddening. The other two spectral windows center on two spot-sensitive molecular absorption features: TiO band ($\lambda = 0.845$–0.870 μm) and the Wing-Ford FeH band ($\lambda = 0.985$–1.02 μm). We note that both of the molecular features are included within the larger spectral window. Given the comparatively large wavelength coverage of the $F_{0.8-1.35\ \mu m}$ removing either or both of the features from the window while performing the fitting routine (see below) affects the $\chi^2_{\rm red}$ values[11] on the order of 0.01%. Therefore, we simply perform the fits to this window without excluding the TiO and FeH absorption features. We will refer to these three spectral regions as spot indicators or indicators as shorthand.

An initial round of fits between the composite models and the target data were performed using the Levenberg–Marquardt minimization algorithm found in *lmfit* (Newville et al. 2014). The $\chi^2_{\rm red}$ values for these fits are systematically large due to the noise in the composite models and the consistently poor fits to the atomic absorption features. The $\chi^2_{\rm red}$ values did not exactly follow a normal distribution. The two-temperature models with $f_{\rm spot}$ that possessed the lowest $\chi^2_{\rm red}$ values were then used as the starting point for the walkers in an *emcee* Markov Chain Monte Carlo (MCMC) sampler (Foreman-Mackey et al. 2013). The MCMC procedure probed the posterior probability density function of $f_{\rm spot}$. In practice, the posterior probability density functions resembled normal distributions with maxima that closely corresponded to the models with the lowest $\chi^2_{\rm red}$ values. We have adopted the 1σ widths of these distributions as the uncertainties in $f_{\rm spot}$. This was performed for every observation and all parameter space, yielding the uncertainties in $f_{\rm spot}$.

For the three different spot indicators, we find good agreement between the best-fit model parameters, $T_{\rm phot}$, $T_{\rm spot}$, and $f_{\rm spot}$ constrained by the $F_{0.8-1.35\ \mu m}$ spectral window and TiO feature.

In Figure 2, we graphically illustrate the goodness of fit by presenting comparisons of one LkCa 4 spectrum to three composite models with different $f_{\rm spot}$ values in the 0.8–1.35 μm window. By visual inspection, the K5V$_p$+ M5V$_s$ model with $f_{\rm spot} = 0.88$ and $\chi^2_{\rm red} \approx 2.3$ is an overall

---

[10] The spectra in the SpeX Library have a short-wavelength cutoff at 0.8 μm because they were collected prior to the 2014 SpeX upgrade to a Hawaii-2RG detector, which pushed the sensitivity down to 0.7 μm.
[11] All χ^2 values presented in the paper are reduced χ^2 values regardless of the subscript.
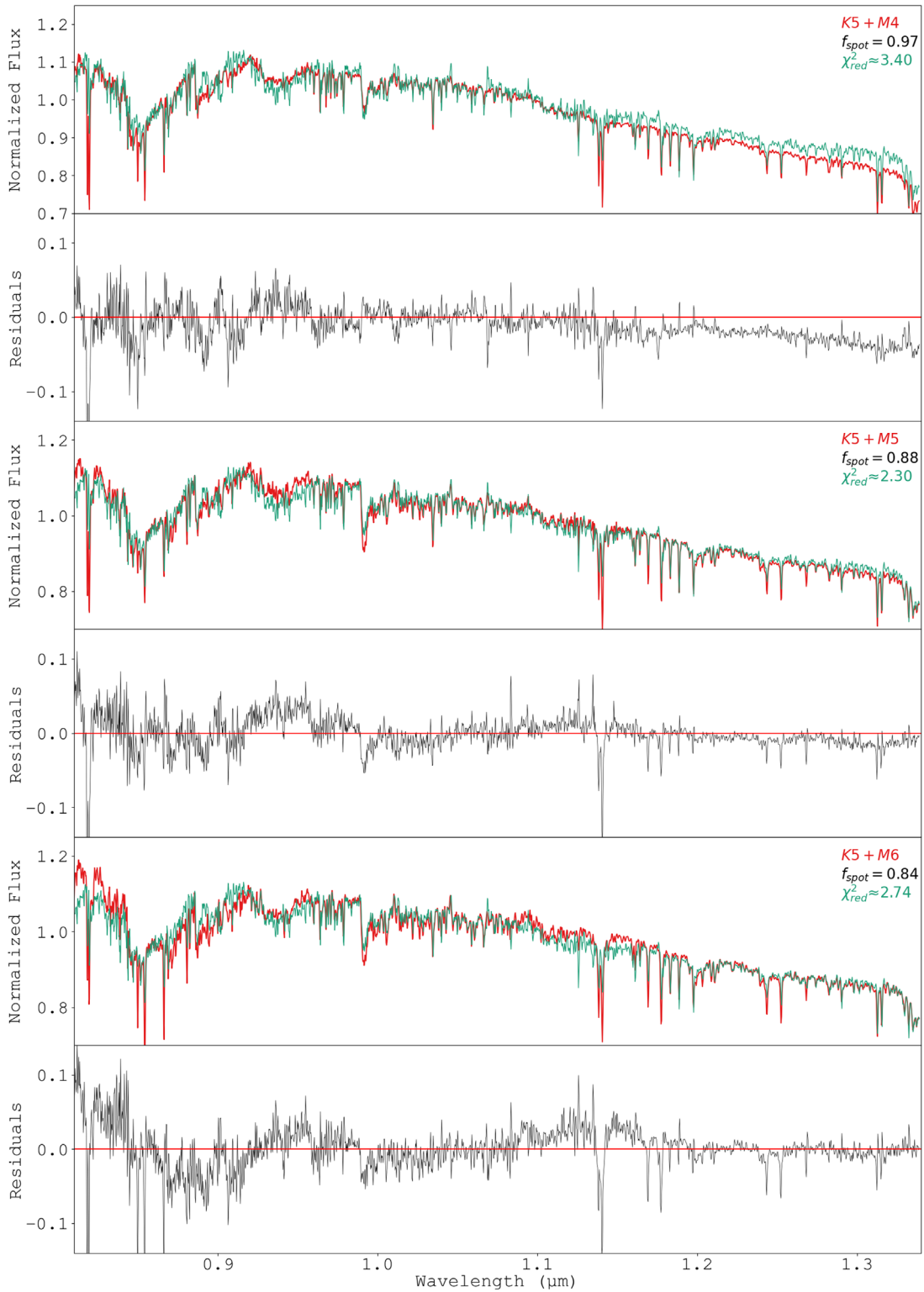
Figure 2. (Top) A dereddened LkCa 4 spectrum (green; $\phi = 0.000$) compared to the best-fit empirical composite spectra K5V$_p$+M4V$_s$ (red). Beneath are residuals plotted with respect to zero (red line). (Middle) and (Bottom) These plots are similar comparisons for the best fits using K5V$_p$+M5V$_s$ and K5V$_p$+M6V$_s$ models, respectively. The χ^2_{red} values were calculated in the 0.8–1.35 μm region.

better fit than the K5V$_p$+M4V$_s$ and K5V$_p$+M6V$_s$ models. For a difference in χ^2_{red} of ~1.1 and 0.44, significant differences in the residuals and the quality of the fits to the strengths of the TiO features and the general shapes of the 0.8–1.35 μm region of the spectra are evident. Similar to the other two-temperature models presented in Bary & Petersen

(2014), atomic absorption features are not well fit and contribute to the large χ^2_{red} as compared to the fits to the TiO or FeH features. Similar differences between the goodness of fit for the K7V$_p$+M4V$_s$, K7V$_p$+M5V$_s$, and K7V$_p$+M6V$_s$ models are observed with the K7V$_p$+M5V$_s$ producing the lowest χ^2 value.

Figure 3. (Top left) A dereddened LkCa 4 spectrum (green; $\phi = 0.000$) and the best-fit empirical composite spectrum with K5V$_p$+M3V$_s$ (red) plotted over the wavelengths corresponding to the FeH window ($l\lambda = 0.985$–$1.02\ \mu$m). (Bottom left) Plotted are the residuals of the fit. (Top middle, top right, and far right) Similar plots comparing the best fits to the FeH feature for the K5V$_p$+M4V$_s$, K5V$_p$+M5V$_s$, and K5V$_p$+M6V$_s$ models, respectively.

It is apparent in Figure 2, that the models do not fit the FeH feature in a predictable manner or one that is consistent with the other spot indicators. On average over the 12 epochs of observations, the FeH fits point to three possible best-fit models with considerably different values for $f_{\rm spot}$. For the K5V$_p$+M3V$_s$ model, the value of $f_{\rm spot}$ is 1.0 essentially selecting an M3V spectrum as the best fit to all 12 epochs. By contrast, the K5V$_p$+M5V$_s$ and K5V$_p$+M6V$_s$ models were equally good fits with $f_{\rm spot}$ values falling in the range of 0.72–0.85 over the 12 epochs. Similar behavior of the FeH fits was observed for the models in which the K5V was replaced with a K7V standard. The spot filling factors decreased as expected for a model with a cooler photosphere. To illustrate the goodness of fit to the FeH feature, we present a similar plot for the FeH comparing four model fits in Figure 3. The K5V$_p$+M4V$_s$ fits are the poorest due to the mismatch between the model and the data between 0.985 and 0.990 μm. The other three models do a far better job of fitting these short wavelengths and differ mostly in the way they fits the small components of the feature. The similarities between the other three fits and the outlier nature of the K5V$_p$+M4V$_s$ points to a potential problem with the M4V standard. If this is the case, then the FeH feature may fit all four of these models equally well over a range of filling factors rendering it a less useful spot indicator than $F_{0.8-1.35\ \mu{\rm m}}$ and TiO. Therefore, we will treat the best-fit models based on these spot indicators as the most

reliable, but will include model parameters associated with the FeH indicator in the following discussion where we believe it is useful and instructive.

In Table 3, we present the values for $f_{\rm spot}$ values associated with the best-fit models constrained by the TiO and $F_{0.8-1.35\ \mu{\rm m}}$. The values listed for each of the 12 observations correspond to two photospheric templates, $F_\lambda({\rm K5V}_p)$ and $F_\lambda({\rm K7V}_p)$, combined with one spot template, $F_\lambda({\rm M5V}_s)$. The $f_{\rm spot}$ values listed for FeH correspond to the same $F(T_{\rm phot})$ and $F(T_{\rm spot})$ and do not represent the model with the minimum χ^2 values obtained using this indicator. In the Appendix, Tables A1 and A2, we provide a more complete listing of the best-fit $f_{\rm spot}$ values over a larger range of spot temperatures for all three spot indicators.

Why do the spot indicators potentially point toward significantly different $f_{\rm spot}$ values for a given pair of $T_{\rm phot}$ and $T_{\rm spot}$? The most straightforward answer seems to be that the moderate resolution spectra of the FeH feature do not distinguish between the two-temperature models as well as the TiO feature and the large spectral window. We also suspect that the differences in the dissociation energies of TiO and FeH ($D_{\rm TiO} = 7.26$ eV; $D_{\rm FeH} = 2.9$ eV; Wahlbeck & Gilles 1967; Wang & Angelici 1996; respectively) may contribute to this discrepancy. For instance, FeH will not form within the photosphere of a K-type star and will only exist within the cooler spot regions. In addition, there may be some differences

Table 3
$f_{\rm spot}$ Values for the K5V$_p$+M5V$_s$ and K7V$_p$+M5V$_s$ Models

Phase (ϕ)	$f_{\rm spot}$(K5V$_p$+M5V$_s$)			$f_{\rm spot}$(K7V$_p$+M5V$_s$)		
	$F_{0.8-1.35\ \mu m}$	TiO	FeH	$F_{0.8-1.35\ \mu m}$	TiO	FeH
0.000	0.88 ± 0.04	0.86 ± 0.01	0.80 ± 0.02	0.85 ± 0.04	0.83 ± 0.02	0.68 ± 0.03
0.028	0.86 ± 0.04	0.88 ± 0.02	0.78 ± 0.03	0.84 ± 0.04	0.85 ± 0.02	0.67 ± 0.03
0.054	0.88 ± 0.04	0.89 ± 0.01	0.80 ± 0.02	0.86 ± 0.04	0.86 ± 0.01	0.71 ± 0.03
0.183	0.89 ± 0.04	0.92 ± 0.01	0.85 ± 0.02	0.87 ± 0.04	0.89 ± 0.01	0.79 ± 0.02
0.209	0.94 ± 0.03	0.92 ± 0.01	0.83 ± 0.03	0.93 ± 0.03	0.90 ± 0.02	0.77 ± 0.03
0.295	0.92 ± 0.03	0.92 ± 0.01	0.80 ± 0.03	0.90 ± 0.03	0.89 ± 0.01	0.71 ± 0.03
0.314	0.94 ± 0.03	0.92 ± 0.02	0.80 ± 0.02	0.93 ± 0.03	0.90 ± 0.01	0.68 ± 0.03
0.600	0.87 ± 0.04	0.88 ± 0.02	0.80 ± 0.02	0.85 ± 0.04	0.84 ± 0.02	0.73 ± 0.03
0.620	0.90 ± 0.03	0.89 ± 0.01	0.79 ± 0.03	0.88 ± 0.04	0.87 ± 0.02	0.69 ± 0.03
0.654	0.87 ± 0.04	0.88 ± 0.01	0.75 ± 0.03	0.85 ± 0.04	0.85 ± 0.01	0.63 ± 0.03
0.892	0.79 ± 0.05	0.86 ± 0.02	0.83 ± 0.03	0.77 ± 0.05	0.81 ± 0.02	0.77 ± 0.03
0.914	0.86 ± 0.04	0.86 ± 0.01	0.85 ± 0.02	0.84 ± 0.04	0.83 ± 0.02	0.80 ± 0.03

in magnetic sensitivity as well as the strength of the magnetic fields impacting the line strengths of these molecules. Again with the FeH feature being produced predominantly in the spotted regions and the TiO features formed both within and outside of the spot, we speculate that the relative line strengths of these features to be more complex than can be described by our relatively simple two-temperature models that lack any specific magnetic field parameters. Finally, as described above, the unknown characteristics of the standard stars given their variability and surface magnetic activity may also affect the composite models.

3.2. Correlating f$_{spot}$ Variability with Stellar Rotation

In Figure 4, we present nearly 7 yr of AAVSO V-band photometry collected between UT 2013 December 24 and UT 2020 October 17 along with the best-fit values for $f_{\rm spot}$ for TiO and $F_{0.8-1.35\ \mu m}$ as well as the corresponding values for FeH. All values have been phase folded setting the time of our first observation taken at JD 2458488.71352 as $\phi = 0.0$ and using $P_{\rm rot} = 3.374$ days (Grankin et al. 2008). The periodic variations in the spot filling factors are positively correlated with the periodic variability in the V-band light curve just as one would expect if the V-band variability were due to spots rotating with the surface of the star. Despite the differences in the absolute values of $f_{\rm spot}$ derived from the TiO, $F_{0.8-1.35\ \mu m}$, and FeH for models with similar values of $T_{\rm phot}$ and $T_{\rm spot}$, the variations within those values correlate with rotational phase (Figure 4).

Given what is known about spot lifetimes on young, active stars, we assume that the spot complex(es) on LkCa 4 are stable during the five nights over which these data were collected. Therefore, we conclude that the observed variability in the instantaneous $f_{\rm spot}$ values is due to the rotation of the star and not due to periodic changes in the total spot coverage or the spot temperatures. In addition, we also rule out contributions to the variability from circumstellar material including phenomena such as inner disk warps and/or accretion flares (Covey et al. 2021) based on the lack of evidence for a circumstellar disk and accretion activity in the LkCa 4 system (e.g., Andrews & Williams 2005).

3.2.1. Predicting ΔV from Best-fit Model Parameters

Next we test whether or not our best-fit spotted star models can reproduce the V-band variability observed in the AAVSO light curve from UT 2019 given that the time frame aligns with
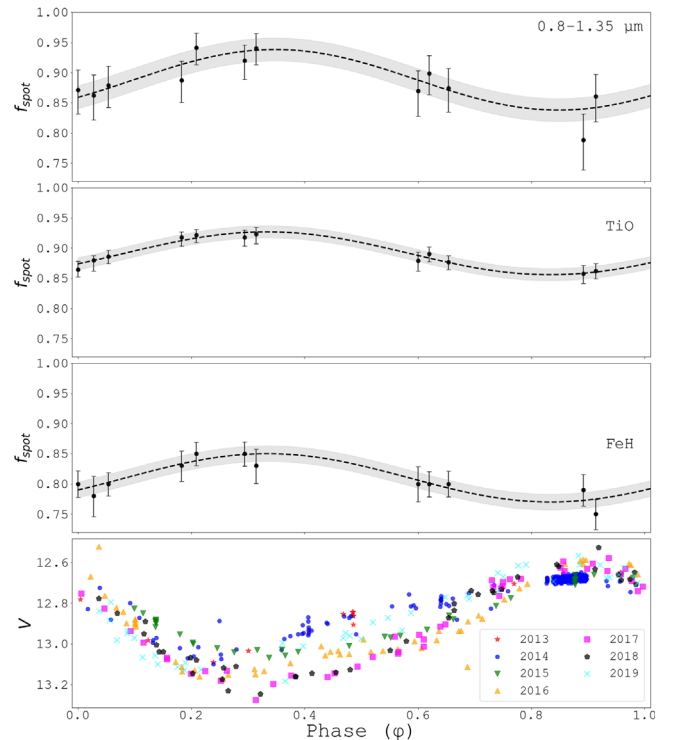
Figure 4. (A) Plotted as a function of rotational phase are the spot filling factors from the best-fit model, K5V$_p$+M5V$_s$, to the $F_{0.8-1.35\ \mu m}$ indicator for all 12 LkCa 4 spectra with $A_V = 0.3$. The dashed line represents a sinusoidal fit to the filling factors, while the gray-shaded region represents the 1σ weighted uncertainty of the fit. (B) Same plot for TiO. (C) Same plot for FeH. (D) The phase-folded AAVSO V-band light curve made with 7 yr of data.

the SpeX observations. We calculated the minimum to maximum V-band variability, ΔV, using the following equation:

$$\Delta V_{\rm calc} = \log\left(\frac{\int_V [(1 - f_{\rm max})F_\lambda(T_p) + f_{\rm max}F_\lambda(T_s)]S_V(\lambda)d\lambda}{\int_V [(1 - f_{\rm min})F_\lambda(T_p) + f_{\rm min}F_\lambda(T_s)]S_V(\lambda)d\lambda}\right),$$

(2)

where $F_\lambda(T_p)$ and $F_\lambda(T_s)$ are the flux densities of the photosphere and spot components, respectively, $f_{\rm max}$ and $f_{\rm min}$ are the maximum and minimum spot filling factors, and $S_V(\lambda)$ is the transmissivity of the Johnson–Cousins V-band filter as

Table 4
$f_{\rm spot}^{\rm mean}$, $f_{\rm spot}^{\rm amp}$, and $\Delta V_{\rm calc}$ Values

Indicator	Model	$f_{\rm spot}^{\rm mean}$	$f_{\rm spot}^{\rm amp}$	$\Delta V_{\rm calc}$
$F_{0.8-1.35\mu m}$	$K5V_p+M5V_s$	0.89 ± 0.02	0.05 ± 0.02	$0.80^{+0.15}_{-0.11}$
TiO	⋯	0.89 ± 0.01	0.04 ± 0.01	$0.56^{+0.10}_{-0.07}$
$F_{0.8-1.35\mu m}$	$K7V_p+M5V_s$	0.87 ± 0.02	0.06 ± 0.02	$0.66^{+0.13}_{-0.09}$
TiO	⋯	0.86 ± 0.01	0.04 ± 0.02	$0.46^{+0.09}_{-0.06}$

defined in the General Catalog of Photometric Data and revised by Mann & von Braun (2015).

We used BT-Settl(CIFIST) (Allard 2014) synthetic spectra over the relevant wavelengths to represent the $F_\lambda(T_p)$ and $F_\lambda(T_s)$ contributions to the V-band magnitude. We calculated four values of $\Delta V_{\rm calc}$, one for each of the $f_{\rm spot}$ values derived from the $F_{0.8-1.35\mu m}$ and TiO indicators for models: $K7V_p+M5V_s$ and $K5V_p+M5V_s$. Values for the mean spot filling factor, $f_{\rm spot}^{\rm mean}$, and its amplitude, $f_{\rm spot}^{\rm amp}$, were extracted from a sinusoidal fit to the phase-folded $f_{\rm spot}$ curves in Figure 4. These values are listed in Table 4.

The observed value for the min-to-max variability in the 2019 AAVSO light curve, $\Delta V_{\rm obs} = 0.526 \pm 0.032$, agrees to within the uncertainties of $\Delta V_{\rm calc} = 0.56^{+0.10}_{-0.07}$ and $\Delta V_{\rm calc} = 0.46^{+0.09}_{-0.06}$ calculated for the $f_{\rm spot}$ values associated with the TiO indicator and the best-fit models, $K5V_p+M5V_s$ and $K7V_p+M5V_s$, respectively. The $f_{\rm spot}^{\rm amp}$ values constrained by the $F_{0.8-1.35\mu m}$ indicator give a slightly larger $\Delta V_{\rm calc}$ than the observed value for both models. The large $f_{\rm spot}^{\rm mean}$ values combined with a larger $f_{\rm spot}^{\rm amp}$ leads to a significant increase in the magnitude of the variation placing the corresponding $\Delta V_{\rm calc}$ values slightly above the observed value.

The agreement between the amplitudes of variations in the spot sizes and the value of ΔV for the TiO indicator provides a reasonable consistency check for the two-temperature model parameters $f_{\rm spot}$, $T_{\rm spot}$, and $T_{\rm phot}$.

3.2.2. Year-to-year Variations of Spot Coverage

The 2013–2019 AAVSO light curve presented in Figure 4(d) possesses a few interesting aspects that suggest the modulation and possible evolution of the spot complexes during this time period. The phase-folded light curve possesses a vertical width of $\delta V = 0.1$–0.2 mag at all phases, though it appears to be largest near $\phi = 0.5$. Such a modulation in δV indicates that the average spot coverage of the stellar surface has changed over this time frame. The slight asymmetry of the variations in the vertical width, particularly between $\phi = 0.2$ and 0.4 suggests an offset or shift in rotational phase, likely indicating a slight alteration in the timing of the minima and maxima over year-long timescales. We estimate the shift in rotational phase to vary between $\delta\phi \sim 0.008$ and $\delta\phi \sim 0.084$ over the 7 yr period. Given the small uncertainties in the photometric measurements, these variations in the phased light curve are likely real features. We do not interpret these phase shifts necessarily as a change in the accepted 3.374 day rotation period of the star. Instead, we believe that they are most likely the result of the spots or spot complexes forming and dissipating at or migrating to different latitudes and/or longitudes. Similar and even more substantive secular changes to the spot coverage were highlighted in three decades of LkCa 4 observations (UT 1986–2016) presented in GS17.
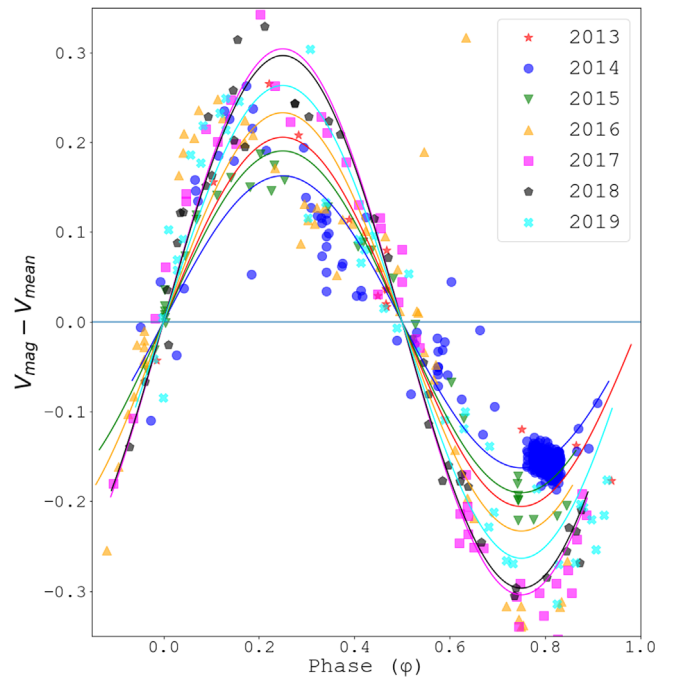
Figure 5. Plotted are seven phase-folded AAVSO light curves from 2013–2019 representing each calendar year. The mean V-band magnitude for each year has been subtracted. Shifts in rotational phase have been removed. The solid lines represent the best-fit sinusoidal functions. The changes in the full photometric variability (minimum to maximum) range between 0.30 and 0.60 mag.

Working from the photometry and assuming that the $T_{\rm phot}$ and $T_{\rm spot}$ remain constant over time, we can use $V_{\rm mean}$ and $\Delta V_{\rm obs}$ in the AAVSO data to estimate $f_{\rm spot}^{\rm mean}$ and $f_{\rm spot}^{\rm amp}$ in previous years. Assuming that the spot coverage is relatively constant on a year-long timescale, the AAVSO photometry from UT 2013–2019 was divided in 1 yr periods. In Figure 5, we present each of the 7 yr long light curves with a best-fit sinusoidal function determined using the same minimization and MCMC algorithm adopted for the spectral fitting. For each light curve, $V_{\rm mean}$ has been subtracted to permit a direct comparison of the year-to-year variations of the amplitude. In addition, small shifts in rotational phase measured relative to the minima and maxima of the UT 2019 curve also have been removed. The values for $V_{\rm mean}$, $\Delta V_{\rm obs}$, and $\Delta\phi$ are listed in Table 5.

In order to determine $f_{\rm spot}^{\rm mean}$ and $f_{\rm spot}^{\rm amp}$ from previous years of V-band data, we associate the value for $f_{\rm spot}^{\rm mean}$ derived from our models with $V_{\rm mean}$ from 2019. Differences between the UT 2019 $V_{\rm mean}$ and previous year $V_{\rm mean}$ are used to determine the values of $f_{\rm spot}^{\rm mean}$. The ΔV value measured from the light curve for a previous year can then be used to determine $f_{\rm spot}^{\rm amp}$ (see Table 5).

Also presented are the ratios of the maximum to minimum *photospheric* filling factors, $f_{\rm phot}^{\rm max}/f_{\rm phot}^{\rm min}$. While directly related to the ratio of the values of $f_{\rm spot}$, we include this value to highlight the strong correlation between ΔV and the changes to $f_{\rm phot}$. One can understand the nature of this correlation better by considering two stars that have the same $T_{\rm phot}$ and $T_{\rm spot}$, but possess the different mean filling factors of $f_{\rm spot}^{\rm mean} = 0.7$ and 0.8. For both stars, assume that the filling factors vary by the same amount, $\Delta f_{\rm spot} = 0.1$ or 10%, such that the ranges of filling factors are $0.65 \leqslant f_{\rm spot} \leqslant 0.75$ and $0.75 \leqslant f_{\rm spot} \leqslant 0.85$,

Table 5
AAVSO V-band Photometry, $f_{spot}^{min} \leftrightarrow f_{spot}^{max}$, and $f_{phot}^{max}/f_{phot}^{min}$ Ratios

UT Year	N_{obs}[a]	V_{mean} (mag)	ΔV_{obs} (mag)	Phase Shift[b] $\Delta\phi$	$f_{spot}^{min} \leftrightarrow f_{spot}^{max}$[c] (K5V$_p$+M5V$_s$)	$f_{phot}^{max}/f_{phot}^{min}$[d] (K5V$_p$+M5V$_s$)	$f_{spot}^{min} \leftrightarrow f_{spot}^{max}$[c] (K7V$_p$+M5V$_s$)	$f_{phot}^{max}/f_{phot}^{min}$[d] (K7V$_p$+M5V$_s$)
2013	14	12.825 ± 0.015	0.406 ± 0.053	-0.039 ± 0.014	0.87–0.92	$1.63^{+0.21}_{-0.13}$	0.84–0.91	$1.78^{+0.22}_{-0.14}$
2014	330	12.835 ± 0.003	0.325 ± 0.007	0.008 ± 0.004	0.87–0.91	$1.44^{+0.13}_{-0.08}$	0.85–0.90	$1.50^{+0.13}_{-0.08}$
2015	36	12.880 ± 0.005	0.381 ± 0.013	0.076 ± 0.005	0.86–0.91	$1.56^{+0.16}_{-0.10}$	0.83–0.90	$1.70^{+0.18}_{-0.12}$
2016	54	12.923 ± 0.016	0.463 ± 0.048	0.084 ± 0.014	0.85–0.91	$1.56^{+0.19}_{-0.12}$	0.80–0.90	$2.00^{+0.25}_{-0.09}$
2017	45	12.932 ± 0.006	0.608 ± 0.018	0.053 ± 0.004	0.83–0.92	$2.13^{+0.38}_{-0.23}$	0.79–0.91	$2.33^{+0.38}_{-0.24}$
2018	40	12.916 ± 0.007	0.593 ± 0.018	0.051 ± 0.005	0.84–0.92	$2.00^{+0.33}_{-0.20}$	0.80–0.91	$2.22^{+0.35}_{-0.22}$
2019	43	12.879 ± 0.010	0.526 ± 0.032	0.000 ± 0.008	0.84–0.94	$2.67^{-0.42}_{+0.83}$	0.81–0.92	$2.38^{-0.46}_{-0.28}$

Notes.
[a] Number of AAVSO observations made during the calendar year.
[b] Shift in rotational phase measured with respect to 2019.
[c] Range of f_{spot} values calculated from V-band measurements.
[d] Photospheric filling factor ratios for the corresponding spot filling factors.

respectively. The star with the larger spot coverage would appear dimmer on average with a higher V_{mean} and would exhibit a larger amplitude of variability despite the same change in f_{spot}. The reason being that the photospheric emission dominates the brightness of the star in the V band of even the most heavily spotted stars. Therefore, the amplitude of variability depends most directly on the ratio of the maximum and minimum filling factors of the photosphere, $f_{phot}^{max}/f_{phot}^{min}$ and less on the absolute change in f_{spot}. Hence, a 10% change in f_{spot} for the star with a larger f_{spot}^{mean} leads to a larger fractional change in the portion of the star covered by the hotter photospheric region. Such a change leads to a larger overall dimming/brightening of the star and a larger amplitude of variability.

The secular changes present in the AAVSO data are depicted in Figure 6, which plots the values of (a) V_{mean}, (b) ΔV_{obs}, (c) the extrapolated minimum and maximum values for f_{spot}, and (d) $f_{phot}^{max}/f_{phot}^{min}$ by year. Within uncertainties, we find that the star is brightest when it displays the smallest ΔV. These values for the V_{mean}, the ΔV values, and the filling factor ratios agree with those of GS17, where a roughly twofold increase in the photospheric filling factor is required to cause a $\Delta V = 0.6$.

4. CO Spectral Index Temperatures

The SpeX SXD spectra provide excellent wavelength coverage of the K band, which includes several strong CO bandheads. The strength of the shortest wavelength CO band at 2.29 μm is used as an indicator for T_{eff}, [Fe/H], and log g and often applied to unresolved spectra of stellar populations in clusters and galaxies. Mármol-Queraltó et al. (2008) updated the definition of a CO spectral index for the 2.29 μm feature, which they designate as D_{CO}. Given the impact of spots on spectral type determinations of heavily spotted PMS stars, we apply the D_{CO} index to our spectra of LkCa 4 for comparison.

Following Mármol-Queraltó et al. (2008), we measure the D_{CO} index as the ratio between the average fluxes in two spectral windows in the continuum near the feature ($\lambda_{cont1} = 2.2460$–2.2550 μm and $\lambda_{cont2} = 2.2710$–2.2770 μm) and the average flux in the absorption band ($\lambda_{CO} = 2.2880$–2.3010 μm).

D_{CO} index values and uncertainties were calculated for each of the 12 observations of LkCa 4. The index values fall within the range of 1.1074–1.1147 with a value for the weighted mean

of 1.1111 ± 0.0022. Using the empirical fitting functions provided by Mármol-Queraltó et al. (2008), we assume a metallicity of [Fe/H] = 0.0 and log $g = 3.8$ to find a corresponding value of $T_{eff} = 3755 \pm 76$ K (see Figure 7). Table 6 lists all of the D_{CO} and corresponding T_{eff} values.

The mean temperature is two subclasses later than a K7V (4100 K), the spectral type reported in Donati et al. (2014). The value more closely matches the temperature of 3670 K determined by Herczeg & Hillenbrand (2014). The D_{CO} temperature, lying between the photospheric and spot temperatures and in relatively good agreement with Herczeg & Hillenbrand (2014) value, suggests that the D_{CO} index is somewhat sensitive to the presence of the cool spots. However, we find in the following analysis of spot-corrected temperatures that the D_{CO} temperature is significantly warmer.

5. Spot-corrected T_{eff}, $L_\star$, and SPOTS Evolutionary Models

Next we calculate spot-corrected values for T_{eff} and $L_\star$ from the values derived for f_{spot}^{mean}, T_{phot}, and T_{spot}. First, we adopt f_{spot}^{mean} values and uncertainties from the best-fit composite models, K7V$_p$+M5V$_s$ and K5V$_p$+M5V$_s$, as estimates of the *total* spot coverage of LkCa 4 with the understanding that a portion of the star is never visible due to the inclination of the stellar rotation axis ($i = 35°$; GS17). Values for T_{eff} were calculated using the following:

$$T_{eff} = [T_{phot}^4(1 - f_{spot}) + T_{spot}^4 f_{spot}]^{0.25} \qquad (3)$$

for the model parameters associated with spot indicators: $F_{0.8-1.35\,\mu m}$ and TiO. Adopting a stellar radius of $2.3\,R_\odot$ (GS17), we calculated the corrected values for $L_\star$. The uncertainties on T_{eff} were estimated by assuming one-half of a subclass uncertainty on the spectral types and associated temperatures for both parameters T_{spot} and T_{phot}. The resulting extrema of T_{eff} values were then used to calculate the upper and lower bounds for the corrected $L_\star$ values. The values derived for T_{eff} and $L_\star$ are listed in Table 7.

In Figure 8, the corrected T_{eff} and $L_\star$ values with the uncertainties obtained from the $F_{0.8-1.35\,\mu m}$ indicator are placed on an H–R diagram alongside literature values taken from Donati et al. (2014), Herczeg & Hillenbrand (2014), GS17, and two values derived using empirical relationships (detailed below) found in Flores et al. (2022). While our two data points
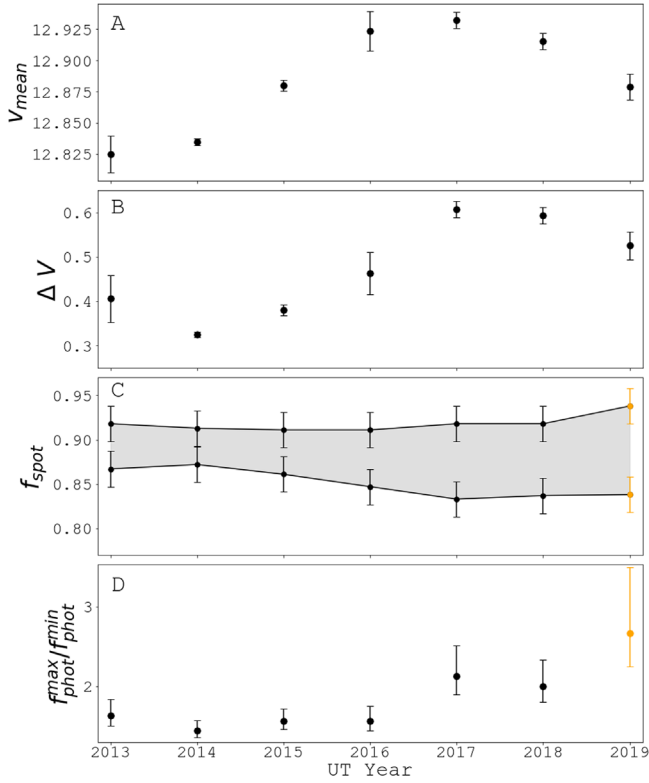
Figure 6. (A) Mean visual magnitudes plotted as a function of year. (B) The min-to-max V-band variability plotted as a function of year. (C) The minimum and maximum spot filling factors for every year assuming a K5V$_p$+M5V$_s$ model. Shaded area represents the total parameter space for $f_{\rm spot}$. The orange data points for 2019 were determined directly from model fits to spectroscopic data. (D) Ratios of maximum and minimum photospheric filling factors plotted for each year also for a K5V$_p$+M5V$_s$ model. Orange data points are same as in (C). (A)–(D) Black data points represent quantities measured directly from AAVSO photometry or a combination of spectroscopic models and photometric data.

with uncertainties reflect only the mean value of $f_{\rm spot}$ with its uncertainties, the gray parallelogram encompasses the entire parameter space associated with $f_{\rm spot}^{\rm min}$ and $f_{\rm spot}^{\rm max}$ measured over the full rotation of the star. Therefore, any single-epoch observation used to correct $T_{\rm eff}$ and $L_\star$ should place the star within the gray parallelogram.

Overlaid are the isochrones and tracks from the Baraffe et al. (2015) standard evolutionary models (orange), as well as those from the Stellar Parameters of Tracks with Starspots (SPOTS) models for $f_{\rm spot} = 0.85$ (black, Somers et al. 2020). The SPOTS evolutionary models incorporate the structural effects of large cool starspots by accounting for phenomena such as the inhibition of convection by strong magnetic fields and the impact spots have on the pressure of the stellar photospheres. SPOTS evolutionary tracks are calculated for low-mass stars with spot filling factors as large as 0.85, making LkCa 4 a perfect candidate for comparison to these models.

First, we note the position of the non-corrected optical $T_{\rm eff}$ and $L_\star$ values from Donati et al. (2014) in Figure 8, which places LkCa 4 between the 0.7 and 0.8 $M_\odot$ standard evolutionary tracks with an age in the range of $\sim$1–3 Myr. The cooler value for $T_{\rm eff}$ from Herczeg & Hillenbrand (2014) shifts the masses down to 0.4 $M_\odot$ and the age to $\sim$0.5 Myr. The rest of the values plotted are in some sense corrected for the existence of spots or cooler regions of the star and shift the
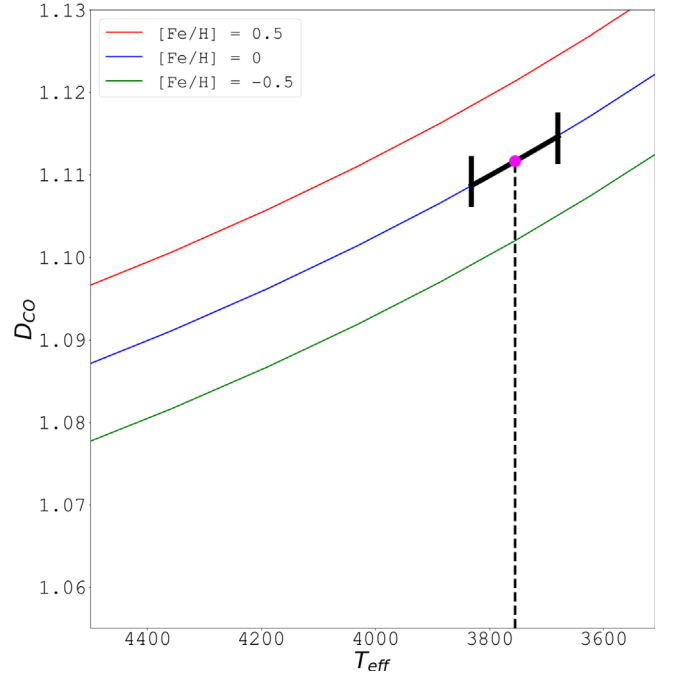
Figure 7. $D_{\rm CO}$ index fitting functions for dwarf stars with metallicities [Fe/H] $= -0.5$, 0.0, and 0.5 for $\log g = 3.8$ are plotted as a function of temperature from Mármol-Queraltó et al. (2008). The filled circle (magenta) represents the weighted mean value for the $D_{\rm CO}$ index. The error bar represents the uncertainty on the weighted mean.

Table 6
$D_{\rm CO}$ Index Values

Phase (ϕ)	$D_{\rm CO}$	Temperature (K)
0.000	1.1130 ± 0.0079	3721 ± 188
0.028	1.1089 ± 0.0094	3826 ± 233
0.054	1.1142 ± 0.0081	3691 ± 189
0.183	1.1071 ± 0.0066	3874 ± 171
0.209	1.1086 ± 0.0097	3834 ± 241
0.295	1.1087 ± 0.0071	3831 ± 179
0.314	1.1074 ± 0.0067	3866 ± 173
0.600	1.1101 ± 0.0075	3795 ± 186
0.620	1.1115 ± 0.0076	3759 ± 185
0.654	1.1145 ± 0.0054	3684 ± 123
0.892	1.1147 ± 0.0101	3679 ± 231
0.914	1.1120 ± 0.0065	3746 ± 158

Table 7
Spot-corrected $T_{\rm eff}$ and $L_\star$ Values

Indicator	Model	$T_{\rm eff}(K)$	Log $(L_\star/L_\odot)$
$F_{0.8-1.35\mu m}$	K5V$_p$+M5V$_s$	3319 ± 90	-0.25 ± 0.05
TiO	...	3312 ± 80	-0.25 ± 0.04
$F_{0.8-1.35\mu m}$	K7V$_p$+M5V$_s$	3263 ± 80	-0.28 ± 0.04
TiO	...	3272 ± 80	-0.27 ± 0.04

values of $T_{\rm eff}$ farther to the right and slightly downward on the H–R diagram.

Relative to the Baraffe+2015 (Baraffe et al. 2015) standard evolutionary models, the corrected values yield lower mass ranges of 0.25–0.30 $M_\odot$ with ages less than 0.5 Myr. These new values represent a shift in mass by a factor of two or
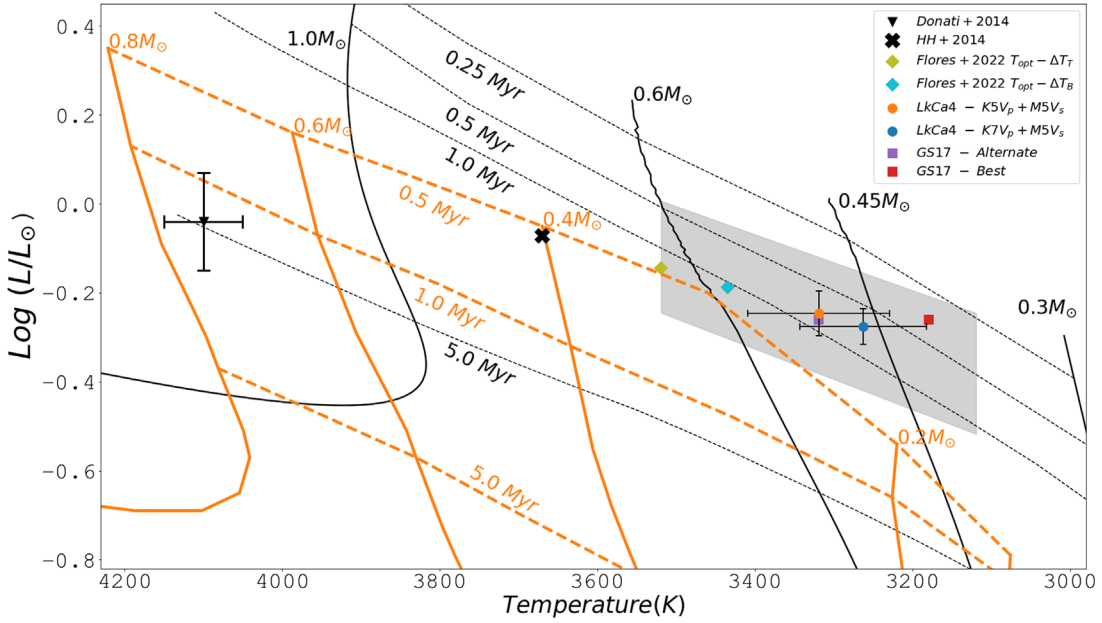
Figure 8. Plotted are the spot-corrected T_{eff} and $L_\star$ values associated with the K5V$_p$+M5V$_s$ (orange circle) and K7V$_p$+M5V$_s$ (blue circle). Error bars on the values come from assuming a half-subclass uncertainty in T_{phot} and T_{spot} and from the uncertainty in the mean f_{spot}. Overlaid are isochrones (dashed) and evolutionary tracks (solid) from Baraffe et al. (2015; orange) and Somers et al. (2020; black) with $f_{\text{spot}} = 0.85$. The gray parallelogram encloses the full range of T_{eff} and $L_\star$ values from the instantaneous filling factors with uncertainties. The solitary black triangle represents the values from Donati et al. (2014). The black cross at $T = 3670\ K$ is from Herczeg & Hillenbrand (2014). The green ($\Delta T_{\text{opt−ir}}$) and cyan (ΔT_B) diamonds represent the T_{eff} values derived from Flores et al. (2022) empirical relations. The red and purple squares are the *best* ($T_{\text{phot}} = 4100$ K, $T_{\text{spot}} = 2750$ K, $f_{\text{spot}} = 0.80$) and *alternate* ($T_{\text{phot}} = 3100$ K, $T_{\text{spot}} = 3000$ K, $f_{\text{spot}} = 0.80$) estimates from GS17.

slightly greater and a decrease in age by a factor between two and six.

Comparing the two sets of evolutionary models, the tracks for the SPOTS models are shifted to cooler temperatures and higher luminosities. Given that the corrected T_{eff} and $L_\star$ moves the star down and to the right, it appears that accounting for the evolutionary effects of spots mitigates some of the shift toward lower masses and younger ages. As such, the corrected placement of LkCa 4 in relation to the $f_{\text{spot}} = 0.85$ SPOTS models increases the mass to a range of 0.45–$0.60\ M_\odot$ and the age to a range of 0.5–1.25 Myr, relative to the Baraffe+2015 (Baraffe et al. 2015) models.

We now turn our attention to the two data points obtained using the empirical relationships derived in Flores et al. (2022). Based on the correlations these authors find between the optical and infrared temperatures as well as the optical temperatures and the strengths of the stellar magnetic fields, they develop two empirical equations for the shifts in temperature: (1) $\Delta T_{\text{opt−ir}} = 0.36 T_{\text{opt}} - 1170$ K and (2) $\Delta T_B = 206B - 135$ K. Note that the uncertainties in the Flores+2022 (Flores et al. 2022) relations are large, so we chose only to use the median values. For both equations, the values for $\Delta T_{\text{opt−ir}}$ and ΔT_B are to be subtracted from T_{opt} to determine T_{eff}. Following Flores et al., we adopted $T_{\text{opt}} = 3670$ K for LkCa 4 from Herczeg & Hillenbrand (2014). For the first relationship, we find a value of $T_{\text{eff}} = 3520$ K and corresponding to $Log (L/L_\odot) = -0.144$. For the second relationship, we assumed the median B-field strength of 1.8 kG reported by Flores et al., likely to be a conservative value for LkCa 4, and find $T_{\text{eff}} = 3435$ K with $Log (L/L_\odot) = -0.187$. As in all cases, the associated values of $L_\star$ were calculated using $R_\star = 2.3\ R_\odot$. Given the large uncertainties on the empirical relations, we are somewhat surprised to see such reasonable agreement between the values these relations predict and the parameter space we find using our two-temperature models. Figure 9 gives a closer view of

the corrected placement of LkCa 4, the GS17 values, and those derived from the Flores+22 (Flores et al. 2022) empirical relations with respect to both SPOTS and standard evolutionary models.

For a subset of stars in the Flores et al. (2022) sample, dynamical masses were available from Atacama Large Millimeter/submillimeter Array observations and were compared to the masses inferred from both optical and infrared temperatures using the Feiden (2016) evolutionary models, which incorporate magnetic effects. They find that the masses inferred from infrared temperatures are much closer to the dynamical masses of the stars than masses inferred from the optical temperatures. However, for the lowest mass stars in their sample, 0.25–$0.4\ M_\odot$, the infrared masses are also overestimations when compared to the dynamical masses by as much as 50%. The interesting and potentially paradigm-shifting implications of this work are that the *spot* component, $F_\lambda(T_{\text{spot}})$, of the two-temperature models appears to be a better approximation of the star's spectral type than the photospheric component, $F_\lambda(T_{\text{phot}})$. Perhaps, this shift in thinking is unsurprising for a PMS star such as LkCa 4 in which the *spot* temperatures were shown to dominate over two-thirds of the stellar surface. The warmer component, in these cases being confined to comparatively smaller regions of the star, behaves more as a *warm* spot on a cooler star than as the stellar photosphere.

The results of these studies strongly suggest that previous determinations of temperatures and luminosities for many young stars are inherently flawed since the optical spectra appear to be dominated by small, warm, non-representative regions of the stellar surface. For such stars, the masses and ages inferred from the warmer temperatures will represent overestimates of masses and ages alike, whether compared to standard evolutionary models or those that take into account magnetic effects and spots. Whether or not these results hint at
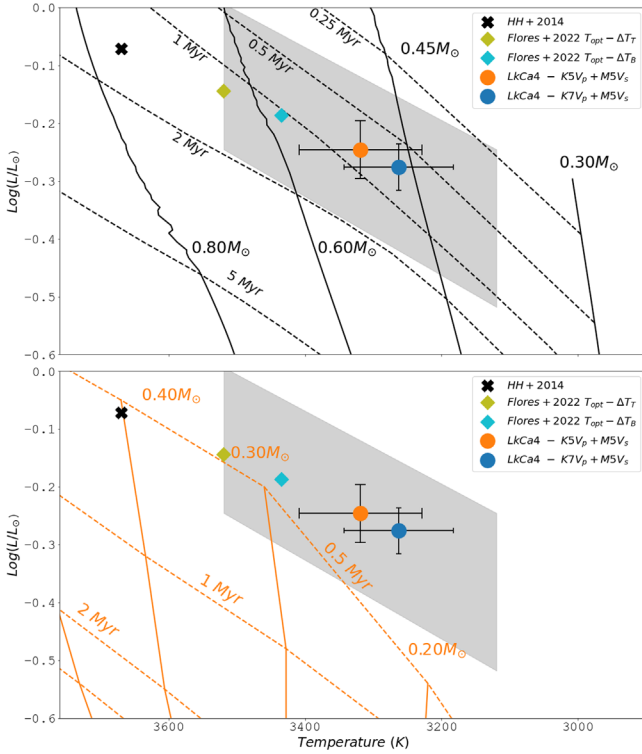
Figure 9. (Top) A close-up view of the corrected $T_{\rm eff}$ and $L_\star$ values for LkCa 4 with respect to the SPOTS models with $f_{\rm spot} = 0.85$ (black lines). The filled orange circle corresponds to the K5V$_p$+M5V$_s$ model. The filled blue circle corresponds to the K7V$_p$+M5V$_s$ model. (Bottom) Same comparison for the Baraffe et al. (2015) models (orange lines). In both plots, the gray parallelogram shows the parameter space for spot-corrected values over the full range of instantaneous filling factors. Plotted values are the same as in Figure 8 with the exclusion of the Donati et al. (2014) data point.

a new physical phenomenon associated with these stars is unclear, but for sources with large discrepancies between optical and infrared colors and temperatures, the spread in masses and ages for objects in a given cluster will be quite large if left uncorrected.

5.1. Impact of Short- and Long-term Variability on Mass and Age Estimates

The short-term, periodic variability of the filling factors due to stellar rotation and the long-term variability associated with changes in the total spot coverage both impact the placement of a star on the H–R diagram and the SPOTS models chosen for comparison. The parameter space enclosed within the solid parallelograms in both Figures 8 and 9 accounts for the full range of variability of the instantaneous filling factors observed over one full rotation of the star. The min-to-max amplitude of the short-term variability in the filling factors is ∼0.1. In the long-term V-band variability inferred from the AAVSO data (Figure 5) spanning nearly a decade and several thousand stellar rotations, we find a comparable level of variability in the total spot filling factor. The parameter space bounded by the parallelogram also constrains the range of ages and masses caused by long-term variations in spot coverage. Therefore, while the application of the SPOTS models is affected by changes to the spot coverage on the order of years, LkCa 4 suggests that over the period of the last decade these models would constrain the mass uncertainties to be $\Delta M_\star = 0.10\ M_\odot$ and age uncertainties to be $\Delta {\rm Age} = 0.625$ Myr.

6. Summary and Conclusion

We illustrate the utility of multi-epoch, medium-resolution spectroscopy combined with two-temperature empirical composite models to accurately constrain (1) the photospheric and spot temperatures, (2) the visual extinction, and (3) the instantaneous and total spot filling factors for the heavily spotted young star LkCa 4. Relying predominantly on the 0.8–1.35 μm region of the SpeX spectra that is sensitive to interstellar extinction and possesses absorption bands associated with TiO and FeH, we fit spectral models of spotted stars with four different photospheric temperatures, eight spot temperatures, and 11 visual extinctions to each of the 12 observations of LkCa 4 collected over five consecutive nights allowing $f_{\rm spot}$ to vary freely between 0.0 and 1.0. Minimizing χ^2 over all possible models, we find two best-fit composite spectra, K5V$_p$+M5V$_s$ and K7V$_p$+M5V$_s$, and $A_V = 0.3$ consistently provide the best fits. Night-to-night variations in the filling factors positively correlate with the historic AAVSO light curves for the system with a rotational period of 3.374 days. Such a correlation demonstrates how multi-epoch spectroscopic observations with moderate resolution can detect the rotation of a spotted star and better constrain the total spot coverage than a single observation.

In addition, we have used the stellar parameters, $T_{\rm phot}$, $T_{\rm spot}$, and $f_{\rm spot}$ returned by the best-fit composite models to predict the magnitudes of V-band variability observed in a similar time frame to when the spectroscopic data was collected and found good agreement. Whether we think of the star as possessing the warmer photosphere with a significant fraction of its surface mottled with cooler regions of suppressed convection activity or being a cooler star with warm spots, the two-temperature models simultaneously explain the observed spectroscopic and photometric variability of the source. Regardless, the observed correlation between magnetic field strengths, anomalous colors, and optical and infrared spectral type mismatches hint at a magnetic origin to these phenomena (Flores et al. 2022).

Assuming that $F_\lambda(T_p)$ and $F_\lambda(T_s)$ remain fairly constant over year to decade-long timescales, the 7 yr time period of AAVSO data studied indicates that the total spot filling factor does not change by more than 5%–10% over this time frame. Small shifts in the rotational phase over year-long time intervals indicate possible migration and evolution of the spots on this time frame.

In comparing the placement of the optical temperatures and luminosities and the corrected values to standard evolutionary models on the H–R diagram, we infer significantly lower masses and younger ages for LkCa 4; a result that agrees well with those from GS17. When compared to the SPOTS models, we find some of the shift to lower masses and younger ages is mitigated. However, the shifts are still significant and important in light of the spread in ages frequently observed for star-forming regions. The range of the corrected values of $T_{\rm eff}$ and $L_\star$ associated with single-epoch observations alone shows considerable spread in mass, $\Delta M_\star = 0.2\ M_\odot$ and $\Delta {\rm Age} \approx$ 1 Myr, and makes the case for more multi-epoch studies of young spotted stars.

Given the apparent ubiquity of optical versus infrared color and spectral type discrepancies for young, low-mass stars, characterizing the impact on previous measurements of $T_{\rm eff}$ and $L_\star$ will be useful for revising and, possibly, refining age and mass inferences for most young stellar clusters. In general, these results should also problematize the notion that a single

spectral type can be assigned to most young stars. For instance, the D_{CO} index points to a T_{eff} that more closely aligns with that determined from optical and NIR TiO features. This value is a few hundred Kelvin warmer than the corrected values from the two-temperature empirical composite models, but several hundred Kelvin cooler than the spectral type based on both optical spectra and color indexes.

The work of Flores et al. (2022) shows that masses inferred from infrared temperatures much more closely align with the dynamical masses of the star, yet they too are likely overestimates for the lowest mass stars in their sample. Their work highlights the need for more comparisons between mass inferences involving evolutionary models and dynamically determined stellar masses. Nonetheless, these results intriguingly point toward a fundamental shift in the phenomenological understanding of the color and spectral type discrepancies.

A collective effort by the star-forming community combining multiwavelength and multi-epoch observations of sources in several nearby star-forming regions would help to characterize total spot coverage, spot, and photospheric temperatures, and determine spot-corrected values for T_{eff} and $L_\star$ across the optical and infrared. Such studies would also permit the application of the newer SPOTS evolutionary models to an extensive sample of PMS stars. As illustrated by Flores et al. (2022), important to these efforts will be the availability of dynamical masses, which will provide useful and necessary constraints on the models as well as additional confirmation or refutation of the phenomenon of large cool starspots. The availability of medium-resolution NIR spectrographs on 3 and 4 m class telescopes makes this methodology an attractive approach to determining spot characteristics for a large number of nearby PMS.

Appendix
Selection of Best-fit Model Parameters and Associated χ^2_{red} Values

In order to determine the best-fit models and values for $F_\lambda(T_{phot})$, $F_\lambda(T_{spot})$, f_{spot}, and A_V, we probed a large parameter space spanning four photospheric templates, eight spot templates, 11 visual extinctions, and filling factors freely varying between 0.0 and 1.0. In Tables A1 and A2, we report the best-fit f_{spot} and associated χ^2_{red} values determined from the three spot indicators for each of the 12 observations. Values are listed for the two best photospheric templates K5V$_p$ and K7V$_p$ combined with six of the eight spot templates. All have been calculated using $A_V = 0.3$.

For both the $F_\lambda(K5V_p)$ and $F_\lambda(K7V_p)$ model fits, we find that the warmest (M1V and M2V) and coolest (M7V and M8V) spot templates produce the largest χ^2_{red} values and the poorest fits for both TiO and $F_{0.8-1.35\mu m}$ spot indicators. Models constructed with M4V$_s$, M5V$_s$, and M6V$_s$ spot templates produce substantially better fits. For each of the six possible composite models and each of the three spot indicators, we calculated the mean χ^2_{red} values over the 12 observations. The K5V$_p$+M5V$_s$ and K7V$_p$+M5V$_s$ models possess both the lowest mean χ^2_{red} values (with the value for the K5V$_p$ models being marginally better than the K7V$_p$) and the smallest standard deviations from the mean suggesting these models are consistently the best fits to the 12 observations spread over five nights.

Table A1

$f_{\rm spot}$ and $\chi^2_{\rm red}$ Values for the K5V$_p$ Template Models

Phase	K5V$_p$+M3V$_s$						K5V$_p$+M4V$_s$						K5V$_p$+M5V$_s$						K5V$_p$+M6V$_s$						K5V$_p$+M7V$_s$						K5V$_p$+M8V$_s$					
	$F_{0.8-1.35\,\mu m}$		TiO		FeH		$F_{0.8-1.35\,\mu m}$		TiO		FeH		$F_{0.8-1.35\,\mu m}$		TiO		FeH		$F_{0.8-1.35\,\mu m}$		TiO		FeH		$F_{0.8-1.35\,\mu m}$		TiO		FeH		$F_{0.8-1.35\,\mu m}$		TiO		FeH	
ϕ	$f_{\rm spot}^{\rm best}$	$\chi^2_{\rm red}$	$f_{\rm spot}^{\rm best}$	$\chi^2_{\rm red}$	$f_{\rm spot}^{\rm best}$	$\chi^2_{\rm red}$	$f_{\rm spot}^{\rm best}$	$\chi^2_{\rm red}$	$f_{\rm spot}^{\rm best}$	$\chi^2_{\rm red}$	$f_{\rm spot}^{\rm best}$	$\chi^2_{\rm red}$	$f_{\rm spot}^{\rm best}$	$\chi^2_{\rm red}$	$f_{\rm spot}^{\rm best}$	$\chi^2_{\rm red}$	$f_{\rm spot}^{\rm best}$	$\chi^2_{\rm red}$	$f_{\rm spot}^{\rm best}$	$\chi^2_{\rm red}$	$f_{\rm spot}^{\rm best}$	$\chi^2_{\rm red}$	$f_{\rm spot}^{\rm best}$	$\chi^2_{\rm red}$	$f_{\rm spot}^{\rm best}$	$\chi^2_{\rm red}$	$f_{\rm spot}^{\rm best}$	$\chi^2_{\rm red}$	$f_{\rm spot}^{\rm best}$	$\chi^2_{\rm red}$	$f_{\rm spot}^{\rm best}$	$\chi^2_{\rm red}$	$f_{\rm spot}^{\rm best}$	$\chi^2_{\rm red}$	$f_{\rm spot}^{\rm best}$	$\chi^2_{\rm red}$
0.000	1.00	4.37	1.00	1.40	1.00	1.56	0.97	3.40	0.92	1.88	1.00	2.04	0.88	2.30	0.86	1.50	0.80	1.65	0.84	2.74	0.88	2.34	0.76	1.41	0.86	3.48	0.87	2.59	0.73	2.14	0.83	5.23	0.91	2.83	0.71	1.99
0.028	1.00	3.65	1.00	1.43	1.00	1.17	0.96	3.35	0.93	1.58	1.00	1.53	0.87	2.21	0.87	1.37	0.78	1.28	0.83	2.66	0.88	2.32	0.75	1.23	0.85	3.48	0.88	2.72	0.71	1.92	0.83	4.78	0.92	2.76	0.69	1.87
0.054	1.00	4.89	1.00	1.75	1.00	1.49	0.98	2.66	0.95	1.61	1.00	1.87	0.89	2.28	0.88	1.27	0.80	1.47	0.85	2.66	0.91	1.93	0.76	1.39	0.86	2.90	0.90	2.33	0.73	2.03	0.84	4.46	0.92	2.58	0.71	1.95
0.183	1.00	11.70	1.00	3.62	1.00	2.56	0.98	6.06	0.98	2.40	1.00	2.94	0.89	3.31	0.92	1.98	0.85	2.45	0.85	3.95	0.91	2.96	0.81	2.49	0.87	4.53	0.91	3.96	0.77	3.67	0.84	6.95	0.93	4.12	0.73	3.51
0.209	1.00	4.26	1.00	1.70	1.00	1.38	1.00	3.05	0.99	1.81	1.00	1.80	0.95	2.15	0.92	1.40	0.83	1.52	0.89	2.68	0.91	2.30	0.80	1.45	0.90	3.26	0.91	2.54	0.76	2.17	0.88	5.21	0.93	2.72	0.73	2.03
0.295	1.00	9.70	1.00	2.52	1.00	2.31	1.00	4.70	0.93	2.22	1.00	2.67	0.92	3.48	0.87	1.82	0.80	2.06	0.88	4.06	0.88	2.79	0.76	1.97	0.89	4.31	0.88	3.49	0.73	3.03	0.86	5.55	0.92	3.71	0.71	2.95
0.314	1.00	8.46	1.00	2.10	1.00	1.64	1.00	4.43	0.95	1.58	1.00	2.03	0.94	2.58	0.89	1.32	0.80	1.43	0.89	2.89	0.91	2.04	0.76	1.32	0.90	3.34	0.90	2.75	0.73	1.91	0.88	4.94	0.93	2.77	0.69	1.94
0.600	1.00	5.52	1.00	1.41	1.00	1.53	0.97	4.64	0.93	1.85	1.00	1.91	0.88	3.24	0.88	1.45	0.80	1.54	0.84	3.54	0.88	2.42	0.77	1.51	0.86	4.05	0.89	2.91	0.73	2.24	0.83	5.65	0.92	3.03	0.71	2.18
0.620	1.00	6.48	0.99	2.00	1.00	1.47	0.99	3.29	0.91	1.91	1.00	1.90	0.90	2.62	0.86	1.55	0.79	1.59	0.86	3.26	0.87	2.62	0.76	1.52	0.87	3.89	0.86	2.96	0.71	2.32	0.85	6.16	0.91	3.26	0.61	2.19
0.654	1.00	3.90	0.99	1.69	1.00	1.56	0.97	2.99	0.91	1.91	1.00	1.94	0.88	2.02	0.86	1.58	0.75	1.72	0.84	2.78	0.88	2.46	0.72	1.66	0.86	3.53	0.87	2.87	0.68	2.43	0.83	5.38	0.91	2.93	0.61	2.23
0.892	0.97	3.42	1.00	1.38	1.00	1.51	0.89	3.82	0.98	1.96	1.00	1.94	0.81	2.50	0.92	1.61	0.83	1.75	0.78	2.86	0.91	2.58	0.80	1.65	0.80	3.28	0.91	2.81	0.76	2.47	0.78	5.09	0.93	3.17	0.72	2.38
0.914	1.00	4.55	1.00	2.44	1.00	1.80	0.96	4.22	0.99	2.56	1.00	2.31	0.87	3.06	0.92	2.16	0.85	2.14	0.83	4.54	0.92	3.44	0.81	2.18	0.85	5.42	0.92	3.70	0.77	2.99	0.82	9.03	0.94	4.30	0.73	2.97

Table A2
$f_{\rm spot}$ and $\chi^2_{\rm red}$ Values for the $K7V_p$ Template Models

Phase	$K7V_p+M3V_s$						$K7V_p+M4V_s$						$K7V_p+M5V_s$						$K7V_p+M6V_s$						$K7V_p+M7V_s$						$K7V_p+M8V_s$					
	$F_{0.8-1.35\ \mu m}$		TiO		FeH		$F_{0.8-1.35\ \mu m}$		TiO		FeH		$F_{0.8-1.35\ \mu m}$		TiO		FeH		$F_{0.8-1.35\ \mu m}$		TiO		FeH		$F_{0.8-1.35\ \mu m}$		TiO		FeH		$F_{0.8-1.35\ \mu m}$		TiO		FeH	
ϕ	$f_{\rm spot}^{\rm best}$	$\chi^2_{\rm red}$	$f_{\rm spot}^{\rm best}$	$\chi^2_{\rm red}$	$f_{\rm spot}^{\rm best}$	$\chi^2_{\rm red}$	$f_{\rm spot}^{\rm best}$	$\chi^2_{\rm red}$	$f_{\rm spot}^{\rm best}$	$\chi^2_{\rm red}$	$f_{\rm spot}^{\rm best}$	$\chi^2_{\rm red}$	$f_{\rm spot}^{\rm best}$	$\chi^2_{\rm red}$	$f_{\rm spot}^{\rm best}$	$\chi^2_{\rm red}$	$f_{\rm spot}^{\rm best}$	$\chi^2_{\rm red}$	$f_{\rm spot}^{\rm best}$	$\chi^2_{\rm red}$	$f_{\rm spot}^{\rm best}$	$\chi^2_{\rm red}$	$f_{\rm spot}^{\rm best}$	$\chi^2_{\rm red}$	$f_{\rm spot}^{\rm best}$	$\chi^2_{\rm red}$	$f_{\rm spot}^{\rm best}$	$\chi^2_{\rm red}$	$f_{\rm spot}^{\rm best}$	$\chi^2_{\rm red}$	$f_{\rm spot}^{\rm best}$	$\chi^2_{\rm red}$	$f_{\rm spot}^{\rm best}$	$\chi^2_{\rm red}$	$f_{\rm spot}^{\rm best}$	$\chi^2_{\rm red}$
0.000	1.00	4.37	1.00	1.40	1.00	1.56	0.96	3.65	0.92	1.80	1.00	2.02	0.86	2.68	0.86	1.54	0.68	1.67	0.82	3.28	0.88	2.14	0.65	1.53	0.83	4.23	0.87	2.57	0.62	2.19	0.81	6.56	0.91	2.75	0.59	2.06
0.028	1.00	3.65	1.00	1.43	0.99	1.17	0.95	3.31	0.93	1.50	1.00	1.53	0.85	2.45	0.87	1.43	0.67	1.40	0.81	2.98	0.88	2.01	0.62	1.39	0.83	3.71	0.88	2.50	0.59	1.99	0.80	5.70	0.92	2.61	0.56	2.08
0.054	1.00	4.89	1.00	1.70	1.00	1.49	0.97	2.71	0.95	1.75	1.00	1.87	0.87	2.51	0.88	1.60	0.71	1.54	0.82	2.98	0.91	2.09	0.67	1.50	0.84	3.31	0.90	2.51	0.62	2.11	0.81	5.25	0.92	2.69	0.59	2.01
0.183	1.00	11.70	1.00	2.52	1.00	2.56	0.98	6.06	0.98	2.19	1.00	2.94	0.88	3.46	0.92	1.89	0.79	2.57	0.83	4.45	0.91	2.79	0.73	2.54	0.85	5.19	0.91	3.43	0.69	3.73	0.82	8.31	0.93	3.65	0.65	3.56
0.209	1.00	4.26	1.00	2.10	1.00	1.38	1.00	3.13	0.99	1.56	1.00	1.80	0.93	2.53	0.92	1.30	0.72	1.60	0.87	3.21	0.92	1.99	0.72	1.57	0.89	3.96	0.92	2.43	0.68	2.20	0.86	6.34	0.94	2.59	0.65	2.10
0.295	1.00	9.70	1.00	1.41	1.00	2.31	1.00	4.70	0.98	1.92	1.00	2.67	0.91	3.78	0.92	1.53	0.71	2.14	0.85	4.42	0.91	2.13	0.67	2.07	0.87	4.81	0.91	2.78	0.62	3.11	0.84	6.81	0.93	2.96	0.59	2.93
0.314	1.00	8.46	1.00	2.00	1.00	1.64	1.00	4.43	0.99	1.91	1.00	2.03	0.93	2.65	0.92	1.84	0.68	1.42	0.87	3.16	0.91	2.65	0.65	1.35	0.89	3.72	0.91	3.07	0.61	1.95	0.86	5.68	0.93	3.38	0.58	1.91
0.600	1.00	5.52	1.00	1.69	1.00	1.53	0.96	4.85	0.93	1.93	1.00	1.91	0.86	3.60	0.87	1.79	0.73	1.65	0.81	4.10	0.88	2.34	0.68	1.71	0.83	4.74	0.88	2.90	0.64	2.38	0.81	6.91	0.92	2.99	0.60	2.22
0.620	1.00	6.48	1.00	1.39	0.98	1.47	0.99	3.34	0.95	1.84	1.00	1.90	0.89	2.97	0.89	1.56	0.69	1.69	0.84	3.82	0.91	2.26	0.64	1.70	0.85	4.70	0.90	2.68	0.60	2.44	0.82	7.62	0.93	3.05	0.59	2.28
0.654	1.00	3.90	1.00	2.44	0.96	1.56	0.97	2.90	0.93	2.69	1.00	1.90	0.86	2.34	0.88	2.57	0.63	1.87	0.82	3.21	0.88	3.39	0.60	1.90	0.84	4.37	0.89	3.96	0.54	2.54	0.81	6.88	0.92	4.38	0.51	2.36
0.892	0.96	3.44	0.99	1.75	1.00	1.52	0.88	3.56	0.91	1.54	1.00	1.94	0.78	2.88	0.86	1.22	0.77	1.87	0.75	3.51	0.87	1.82	0.72	1.80	0.78	4.17	0.86	2.24	0.66	2.52	0.75	6.08	0.91	2.53	0.64	2.60
0.914	1.00	4.55	0.99	3.62	1.00	1.84	0.95	4.30	0.91	2.43	1.00	2.31	0.85	3.67	0.86	2.27	0.80	2.30	0.80	5.21	0.88	3.13	0.73	2.27	0.82	7.15	0.87	3.96	0.69	3.09	0.80	10.48	0.91	4.32	0.65	3.01

As discussed in Section 3.1, the FeH indicator does not easily distinguish between the best-fit models, selecting models with warm spots and extremely large filling factors (i.e., essentially single-temperature fits) and those with cooler spots and smaller filling factors equally over nearly all the epochs. In addition, the poorer fits made to the models using an M4V standard to model the spots seem to be an outlier and may reveal something about the nature of the standard (see Figure 3).

ORCID iDs

Facundo Pérez Paolino ⬤ https://orcid.org/0000-0002-4128-7867
Jeffrey S. Bary ⬤ https://orcid.org/0000-0001-8642-5867
Michael S. Petersen ⬤ https://orcid.org/0000-0003-1517-3935
Kimberly Ward-Duong ⬤ https://orcid.org/0000-0002-4479-8291
Benjamin M. Tofflemire ⬤ https://orcid.org/0000-0003-2053-0749
Katherine B. Follette ⬤ https://orcid.org/0000-0002-7821-0695

References

Afram, N., & Berdyugina, S. V. 2015, A&A, 576, A34
Afram, N., & Berdyugina, S. V. 2019, A&A, 629, A83
Alfonso-Garzon, J., Domingo, A., Mas-Hesse, J. M., & Gimenez, A. 2012, A&A, 548, A79
Allard, F. 2014, in IAU Symp. 299, Exploring the Formation and Evolution of Planetary Systems, ed. M. Booth, B. C. Matthews, & J. R. Graham (Cambridge: Cambridge Univ. Press), 271
Andrews, S. M., & Williams, J. P. 2005, ApJ, 631, 1134
Astropy Collaboration, Robitaille, T. P., Tollerud, E. J., et al. 2013, A&A, 558, A33
Baraffe, I., Homeier, D., Allard, F., & Chabrier, G. 2015, A&A, 577, A42
Bary, J. S., & Petersen, M. S. 2014, ApJ, 792, 64
Bouvier, J., Covino, E., Kovo, O., et al. 1995, A&A, 299, 89
Cenarro, A. J., Gorgas, J., Vazdekis, A., Cardiel, N., & Peletier, R. F. 2003, MNRAS, 339, L12
Coelho, P., Barbuy, B., Meléndez, J., Schiavon, R. P., & Castilho, B. V. 2005, A&A, 443, 735
Couture, J., & Hardy, E. 1993, ApJ, 406, 142
Covey, K. R., Larson, K. A., Herczeg, G. J., & Manara, C. F. 2021, AJ, 161, 61
Cushing, M., Vacca, W., & Rayner, J. 2004, PASP, 116, 362
Cushing, M. C., Rayner, J. T., & Vacca, W. D. 2005, ApJ, 623, 1115
Czekala, I., Andrews, S. M., Mandel, K. S., Hogg, D. W., & Green, G. M. 2015, ApJ, 812, 128
D'Antona, F., & Mazzitelli, I. 1994, ApJS, 90, 467
Debes, J. H., Jang-Condell, H., Weinberger, A. J., Roberge, A., & Schneider, G. 2013, ApJ, 771, 45
Donati, J.-F., Hébrard, E., Hussain, G., et al. 2014, MNRAS, 444, 3220
Fang, X.-S., Zhao, G., Zhao, J.-K., & Bharat Kumar, Y. 2018, MNRAS, 476, 908
Feiden, G. A. 2016, A&A, 593, A99
Feigelson, E. D., & Montmerle, T. 1999, ARA&A, 37, 363
Fitzpatrick, E. L. 1999, PASP, 111, 63
Flores, C., Connelley, M. S., Reipurth, B., & Boogert, A. 2019, ApJ, 882, 75
Flores, C., Connelley, M. S., Reipurth, B., & Duchêne, G. 2022, ApJ, 925, 21
Foreman-Mackey, D., Hogg, D. W., Lang, D., & Goodman, J. 2013, PASP, 125, 306

Gershberg, R. E., Katsova, M. M., Lovkaya, M. N., Terebizh, A. V., & Shakhovskaya, N. I. 1999, A&AS, 139, 555
Grankin, K. N. 2013, AstL, 39, 251
Grankin, K. N., Bouvier, J., Herbst, W., & Melnikov, S. Y. 2008, A&A, 479, 827
Gullbring, E., Hartmann, L., Briceno, C., Calvet, N., & Muzerolle, J. 1998, in ASP Conf. Ser. 154, 10th Cambridge Workshop on Cool Stars, Stellar Systems, and the Sun, ed. R. A. Donahue & J. A. Bookbinder (San Francisco, CA: ASP), 1709
Gully-Santiago, M. A., Herczeg, G. J., Czekala, I., et al. 2017, ApJ, 836, 200
Hartigan, P., Edwards, S., & Ghandour, L. 1995, ApJ, 452, 736
Hartman, J. D., Bakos, G. Á, Noyes, R. W., et al. 2011, AJ, 141, 166
Hartmann, L., Herczeg, G., & Calvet, N. 2016, ARA&A, 54, 135
Herbig, G. H., Vrba, F. J., & Rydgren, A. E. 1986, AJ, 91, 575
Herbst, W., Eislöffel, J., Mundt, R., & Scholz, A. 2007, in Protostars and Planets V, ed. B. Reipurth, D. Jewitt, & K. Keil (Tucson, AZ: Univ. Arizona Press), 297
Herbst, W., & Levreault, R. M. 1990, AJ, 100, 1951
Herczeg, G. J., & Hillenbrand, L. A. 2014, ApJ, 786, 97
Hunter, J. D. 2007, CSE, 9, 90
Jones, D. O., & West, A. A. 2016, ApJ, 817, 1
Jones, E., Oliphant, T., & Peterson, P. 2001, SciPy: Open Source Scientific Tools for Python, http://www.scipy.org
Kastner, J. H., Rapson, V., Sargent, B., Smith, C. T., & Rayner, J. 2015, arXiv:1409.7135313
Kenyon, S. J., & Hartmann, L. 1995, ApJS, 101, 117
Kochukhov, O. 2021, A&ARv, 29, 1
Mann, A. W., & von Braun, K. 2015, PASP, 127, 102
Mármol-Queraltó, E., Cardiel, N., Cenarro, A. J., et al. 2008, A&A, 489, 885
Neff, J. E., O'Neal, D., & Saar, S. H. 1995, ApJ, 452, 879
Newville, M., Stensitzki, T., Allen, D. B., & Ingargiola, A. 2014, LMFIT: Non-Linear Least-Square Minimization and Curve-Fitting for Python, v0.8.0, Zenodo, doi:10.5281/zenodo.11813
O'Neal, D., Saar, S. H., & Neff, J. E. 1996, ApJ, 463, 766
Pecaut, M. J., & Mamajek, E. E. 2013, ApJS, 208, 9
Petrov, P. P., Gahm, G. F., Stempels, H. C., Walter, F. M., & Artemenko, S. A. 2011, A&A, 535, A6
Preibisch, T. 2012, RAA, 12, 1
Rayner, J. T., Cushing, M. C., & Vacca, W. D. 2009, ApJS, 185, 289
Rayner, J. T., Toomey, D. W., Onaka, P. M., et al. 2003, PASP, 115, 362
Reiners, A., & Basri, G. 2006, ApJ, 644, 497
Samus', N. N., Kazarovets, E. V., Durlevich, O. V., Kireeva, N. N., & Pastukhova, E. N. 2017, ARep, 61, 80
Schiavon, R. P., Barbuy, B., & Singh, P. D. 1997, ApJ, 484, 499
Shulyak, D., Reiners, A., Nagel, E., et al. 2019, A&A, 626, A86
Shulyak, D., Reiners, A., Seemann, U., Kochukhov, O., & Piskunov, N. 2014, A&A, 563, A35
Soderblom, D. R., Hillenbrand, L. A., Jeffries, R. D., Mamajek, E. E., & Naylor, T. 2014, in Protostars and Planets VI, ed. H. Beuther, R. S. Klessen, C. P. Dullemond, & T. Henning (Tuscon, AZ: Univ. of Arizona Press), 219
Somers, G., Cao, L., & Pinsonneault, M. H. 2020, ApJ, 891, 29
Stelzer, B., Schmitt, J. H. M. M., Micela, G., & Liefke, C. 2006, A&A, 460, L35
Strassmeier, K. G. 2009, A&ARv, 17, 251
Strom, K. M., & Strom, S. E. 1994, ApJ, 424, 237
Vacca, W. D., & Sandell, G. 2011, ApJ, 732, 8
Valenti, J. A., & Johns-Krull, C. 2001, in ASP Conf. Ser. 248, Magnetic Fields Across the Hertzsprung-Russell Diagram, ed. G. Mathys, S. K. Solanki, & D. T. Wickramasinghe (San Francisco, CA: ASP), 179
van der Walt, S., Colbert, S. C., & Varoquaux, G. 2011, CSE, 13, 22
Wahlbeck, P. G., & Gilles, P. W. 1967, JChPh, 46, 2465
Wang, D., & Angelici, R. J. 1996, JAChS, 118, 935
White, R. J., & Ghez, A. M. 2001, ApJ, 556, 265